Lithos 364–365 (2020) 105507

Contents lists available at ScienceDirect

Lithos

journal homepage: www.elsevier.com/locate/lithos

Research Article

Magmatic-hydrothermal processes recorded by muscovite and columbite-group minerals from the Bailongshan rare-element pegmatites in the West Kunlun-Karakorum orogenic belt, NW China

Chang-Ming Xing [a,b,*], Christina Yan Wang [a,b], He Wang [a,b]

[a] Key Laboratory of Mineralogy and Metallogeny, Guangzhou Institute of Geochemistry, Chinese Academy of Sciences, Guangzhou 510460, China
[b] Guangdong Provincial Key Laboratory of Mineral Physics and Materials, Guangzhou 510640, China

ARTICLE INFO

Article history:
Received 31 May 2019
Received in revised form 3 March 2020
Accepted 23 March 2020
Available online 24 March 2020

Keywords:
Muscovite
Columbite-group mineral
Rare metals
Magmatic-hydrothermal process
Bailongshan rare-element pegmatites
West Kunlun-Karakorum orogenic belt
NW China

ABSTRACT

The mineralization of rare-element pegmatites is attributed to complex magmatic-hydrothermal processes such as magma fractionation, fluid exsolution and fluid/melt metasomatism. However, it is still unclear how these processes affect the evolution of pegmatites and the fractionation of rare elements. Here we use the textures and major and trace element compositions of muscovite and columbite-group minerals (CGM) from the newly discovered Bailongshan Li-Cs-Ta (LCT)-type pegmatites in the West Kunlun-Karakorum orogenic belt, NW China, to decipher the magmatic-hydrothermal processes related to enrichment of rare elements. Four major regional zones are recognized in the Bailongshan area; quartz-albite-tourmaline (QAT) zone, quartz-muscovite (QM) zone, quartz-albite-spodumene (QAS) zone and quartz-spodumene (QS) zone. The QAT and QM zones are barren, whereas the QAS and QS zones host six major Li—Rb ore segments (I to VI) along the NWW-SEE strike. From the QM zone through the QAS to the QS zone, the K/Rb ratios of muscovite decrease gradually from 26.0 to 7.8 and CGM has Mn#s increasing from 0.28 to 0.56, consistent with the trend of progressive evolution of the pegmatites. The Ta# profiles across individual CGM grains reveal a three-stage growth process, i.e., from a Nb-rich CGM magmatic stage to a Ta-rich CGM magmatic stage to a Nb-rich CGM hydrothermal stage. High-resolution elemental mapping of primary muscovite from the QAS and QS zones shows that melt metasomatism induced local enrichment of F, Li, Cs and Ta and the precipitation of secondary lepidolite along the rims or cleavages of primary muscovite. In addition, late-stage, F-poor fluid metasomatism caused the release of Fe, Mn, B, Rb and Cs from primary muscovite, and induced complex zoning patterns and crystallization of hydroxylapatite in cleavage planes of primary muscovite. Secondary muscovite has higher Li, Be, B, Rb and Cs and lower Nb than primary muscovite, indicating that these elements may have been partially dissolved and remobilized from primary spodumene, muscovite and CGM into late-stage hydrothermal fluids, from which the secondary muscovite and Nb-rich CGM crystallized. Therefore, the complex zoning patterns and compositional variations of both muscovite and CGM from the Bailongshan pegmatites record a progressive magmatic-hydrothermal process related to the rare-metal mineralization.

1. Introduction

Granitic pegmatites are of great economic importance because they host exceptionally diverse rare-metal mineralization such as Li, Be, Rb, Cs, Nb, Ta, W and Sn (London and Kontak, 2012). They are generally considered to have formed from highly fractionated, volatile-rich, residual magmas of granitic plutons (Černý et al., 2005; Shearer et al., 1992). Highly mobile fluxing components (e.g., H_2O, Li, B, P and F) play a significant role in reducing melt polymerization and lowering the solidus temperature of granitic melts, and are thus critical to rare-metal mineralization (Černý et al., 2005; Halter and Webster, 2004; London, 2014). Although fractional crystallization of magma is conventionally thought to be the major control on the formation of pegmatite, it alone cannot lead to the large fractionation of rare elements (e.g., Nb/Ta <5) of granitic rocks (Ballouard et al., 2016). Experimental studies demonstrate that melt/fluid immiscibility during magmatic-hydrothermal transitions can produce three coexisting phases, including a silicate melt, a hydrosaline melt and a vapor (or fluid) phase, and preferential partitioning of rare elements into the different phases may significantly affect the evolution of pegmatites and associated rare-metal mineralization (Veksler, 2004; Veksler et al., 2002; Veksler and Thomas, 2002). In addition, late-stage melt/fluid metasomatism also plays an important

* Corresponding author at: Key Laboratory of Mineralogy and Metallogeny, Guangzhou Institute of Geochemistry, Chinese Academy of Sciences, Guangzhou 510460, China.
E-mail address: cmxing@gig.ac.cn (C.-M. Xing).

https://doi.org/10.1016/j.lithos.2020.105507
0024-4937/

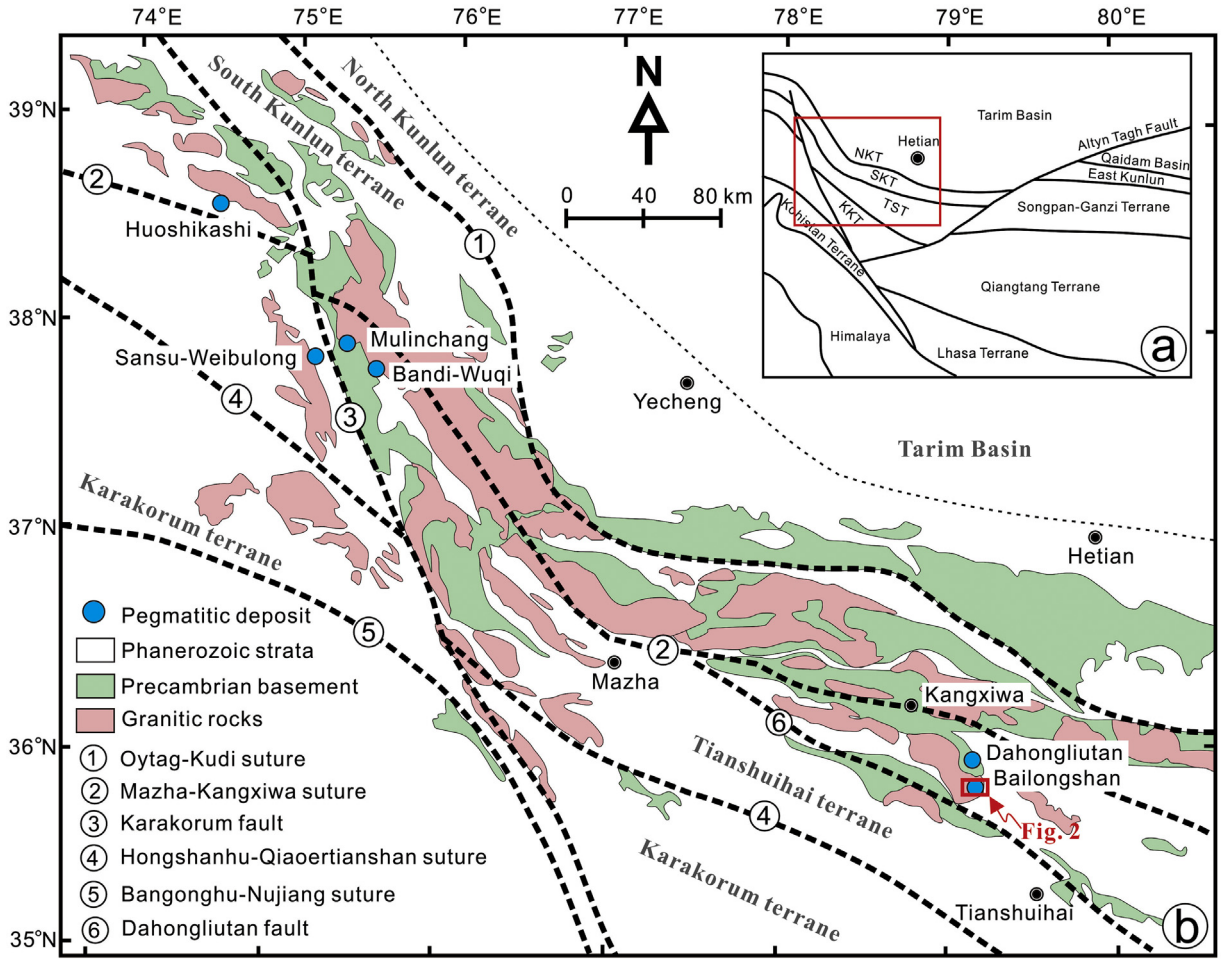

Fig. 1. Geological map showing the distribution of the West Kunlun-Karakorum orogenic belt (a); and the locations of major pegmatite deposits with rare-metal mineralization (b). Modified after Zhang et al. (2016) and Yan et al. (2018).

role in the mobilization and re-deposition of rare elements from primary minerals in pegmatites (Anderson et al., 2013; Van Lichtervelde et al., 2008).

Mica-group minerals are very common in granitic pegmatites (Jolliff et al., 1987; Marchal et al., 2014; Roda-Robles et al., 1995; Wang et al., 2019). They host many rare elements such as Li, Be, Rb, Cs, Ba, Sn, Nb and Ta, and can be taken as diagnostic indicators for pegmatite evolution and rare-metal mineralization (Anderson et al., 2013; Kaeter et al., 2018; Oyarzábal et al., 2009; Van Lichtervelde et al., 2008; Wang et al., 2019; Yin et al., 2019). Columbite-group minerals (CGM, [(Mn, Fe)(Ta, Nb)$_2$O$_6$]) in granitic pegmatites are the major host of Ta and Nb, and their textures and compositions have been used to identify complex magmatic and hydrothermal processes during rare-metal mineralization (Anderson et al., 2013; Kaeter et al., 2018; Zhu et al., 2015). Therefore, a combined study of mica and CGM can provide good constraints on the complex magmatic-hydrothermal processes related to rare-metal mineralization.

The newly discovered Bailongshan pegmatites host economically important Li and Rb mineralization and are a part of the Li mineralized belt in the West Kunlun-Karakorum orogenic belt, NW China (Wang et al., 2017a). The Bailongshan pegmatites, which belong to the lithium-cesium-tantalum (LCT) family of rare-element pegmatites, are also enriched in Be, Nb, Ta and Sn (Wang et al., 2017a, 2020; Yin et al., 2020). In this study we document the textures and compositions of muscovite and CGM from the Bailongshan pegmatites and use these data to constrain the magmatic-hydrothermal processes related to the rare-metal mineralization.

2. Geological background

The West Kunlun-Karakorum orogenic belt along the northwestern margin of the Tibetan plateau (Fig. 1) is considered to have formed by prolonged subduction of the Proto- and Paleo-Tethyan lithosphere and terrane collisions from the early Paleozoic to early Mesozoic (Xiao et al., 2002, 2003). It is mainly composed of four terranes; i.e., the North Kunlun terrane (NKT), the South Kunlun terrane (SKT), the Tianshuihai terrane (TST), and the Karakorum terrane (KKT) (Fig. 1a; Zhang et al., 2019 and references therein). The Tianshuihai terrane, which is bounded by the Mazha-Kangxiwa suture zone on the north and the Hongshanhu-Qiaoertianshan suture zone on the south, hosts six known pegmatite deposits with rare-metal mineralization. These are located in the Huoshikashi, Mulingchang, Sansu-Weibulong, Bandi-Wuqi, Dahongliutan and Bailongshan areas (Fig. 1b), making the region an economically significant zone of Li mineralization (Wang et al., 2017a).

The Tianshuihai terrane consists of sedimentary and metamorphic strata ranging in age from Sinian to Triassic. The Tianshuihai Group of Sinian age is composed of greenschist-facies, chloritoid phyllite, argillite, siltstone, marble and dolomite, whereas the overlying Cambrian Tianshuihu Formation consists chiefly of carbonaceous slate, siltstone, dolomite and limestone. The Silurian Wenquangou Formation is composed of quartz sandstone, with minor silicalite and dacite. Unconformably overlying the Wenquangou Formation is the Triassic Bayan Har Mountain Group, which includes weakly metamorphosed quartz sandstone, sericite-quartz schist and two-mica schist (Wang et al., 2017a). In

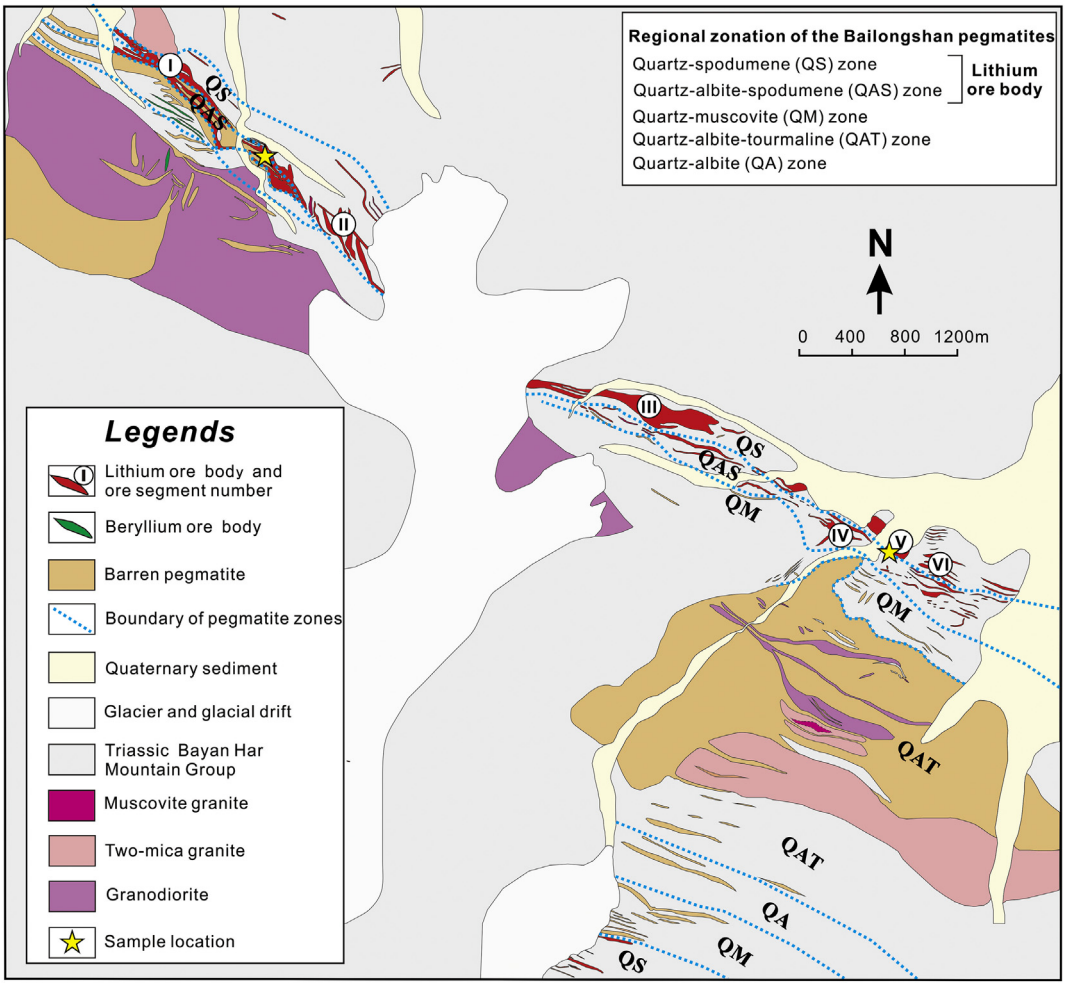

Fig. 2. Geological map showing the distribution of the Bailongshan pegmatites and regional zonation. Modified after Wang et al. (2020).

the Dahongliutan area, more than 7000 pegmatite dykes, many of which host Li-Be-Nb-Ta mineralization, have been emplaced in the Dahongliutan granitic pluton and the Bayan Har Mountain Group (Zhou et al., 2011).

Similar pegmatites occur in the Bailongshan area, ~15 km from the Dahongliutan area (Fig. 1b). These pegmatites have a columbite-tantalite U—Pb age of ca. 208 Ma and are spatially associated with a coeval granodiorite batholith in the northwest and two-mica, granitic plutons in both the northwest and southeast (Wang et al., 2017a, 2020) (Fig. 2). They comprise a number of Li-rich ore bodies and numerous barren pegmatites, which together constitute a giant dyke swarm (Fig. **2**; Wang et al., 2017a).

The Li-rich ore bodies in the Bailongshan pegmatites vary from 46 to 165 *m* in width, extend for more than 3750 *m* along the NWW-SEE strike and dip 65° - 80° NE (Wang et al., 2017a). The barren pegmatites mainly occur south of the ore bodies, and are distributed on both sides of a two-mica granitic pluton in the southeastern part of the Bailongshan area (Fig. 2). Four major textural and mineralogical zones are recognized between the Li-rich and barren pegmatite, which from north to south include a quartz-spodumene (QS) zone, a quartz-albite-spodumene (QAS) zone, a quartz-muscovite (QM) zone and a wide quartz-albite-tourmaline (QAT) zone (Wang et al., 2020). Similar regional zones are also present in the southern part of the Bailongshan area (Fig. 2).

The QAT zone mainly contains fine- to medium-grained quartz, albite, black tourmaline and muscovite (Fig. 3a, b). The tourmaline crystals are locally aligned to form thin, nearly monocrystalline layers (Fig. 3b, c). In addition, clear modal layering occurs in the margin of the QAT zone (Wang et al., 2020). The QM zone mainly contains quartz, muscovite and variable amounts of albite with minor beryl (Fig. 3d) but lacks tourmaline. The QAS zone mainly contains quartz, albite, muscovite and spodumene (Fig. 3e), whereas the QS zone is characterized by spodumene and quartz with minor albite and muscovite (Fig. 3f). Both the QAS and QS zones have pegmatitic textures, with some spodumene crystals up to 10 cm in size; in these zones spodumene can locally reach 40–50 vol% of the rock (Fig. 3e).

Li-rich ore bodies occur mainly in the QAS and QS zones, where they are divided into six segments from I to VI along strike (Fig. 2). Estimated ore reserves of segments I, II and III combined are ~3.45 Mt. of Li_2O and ~176,000 tons of Rb_2O (Wang et al., 2017a), but segments IV, V and VI in the southeastern part of the Bailongshan area are much smaller (Fig. 2). There is little internal zonation within individual pegmatite orebodies (Wang et al., 2020). Beryllium mineralization is only present in a few pegmatites in the northwestern part of the Bailongshan area (Fig. 2).

In this study, samples were collected from the barren QM zone and the orebodies in segments II and V in the QAS and QS zones.

3. Petrography

Spodumene from the rocks of the QAS and QS zones commonly has a curved outline with dissolution and replacement textures (Fig. 4a, b, c). Fine-grained spodumene can be completely replaced by symplectites of

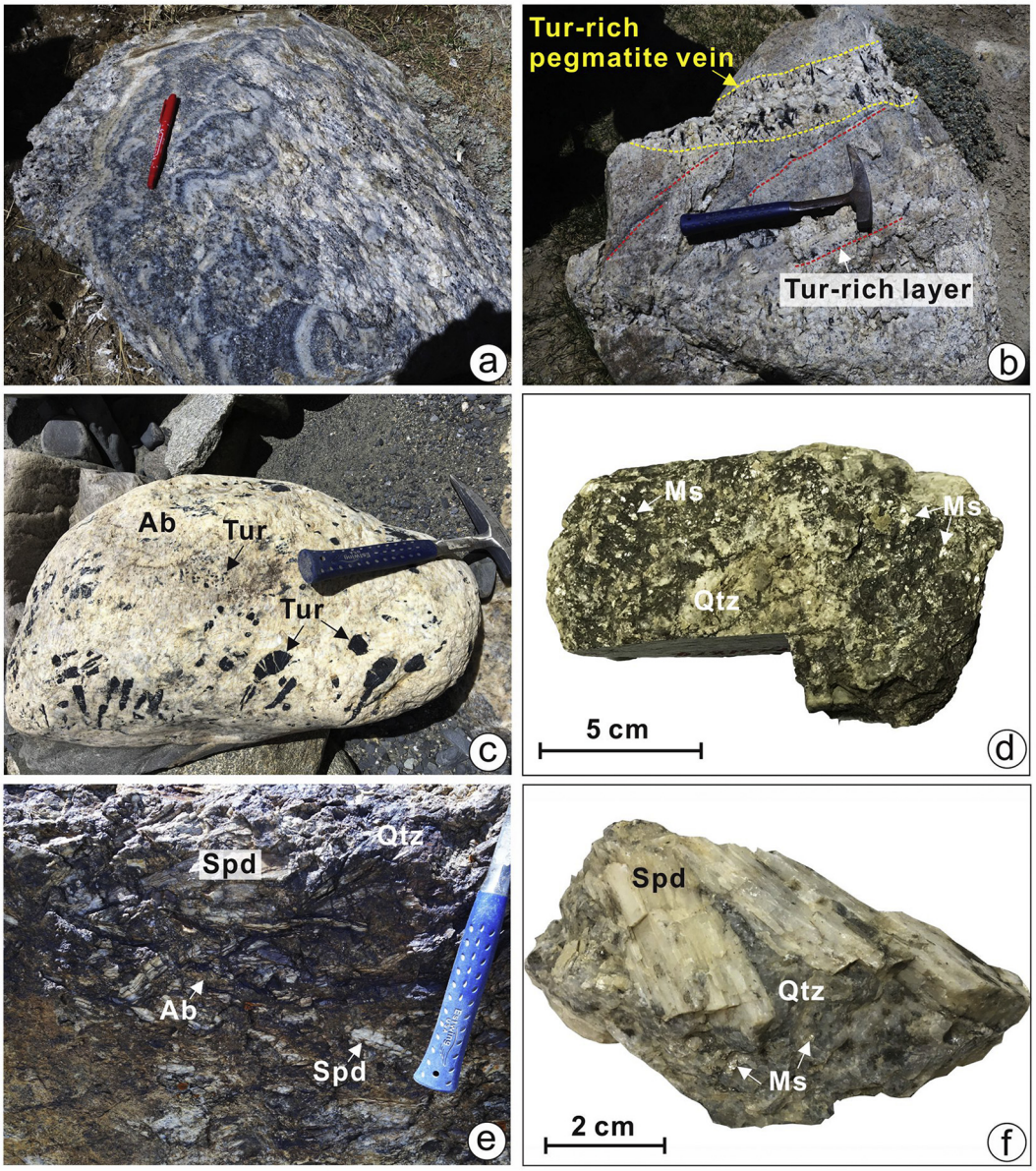

Fig. 3. Field photographs of the Bailongshan pegmatites. (a - b) Outcrop of fine-grained quartz-albite-tourmaline zone showing layered structure and tourmaline-rich layers. Note a pegmatite vein in the fine-grained mineral assemblages. (c) A boulder of the blocky albite-quartz-tourmaline pegmatite showing abundant black tourmaline. (d) A hand specimen from the quartz-muscovite zone. (e) Outcrop of the quartz-albite-spodumene zone showing white, elongated spodumene. (f) A hand specimen from the quartz-spodumene zone showing pegmatitic spodumene associated with grey quartz and fine-grained muscovite. Abbreviations: Ab-albite; Ms-muscovite; Qtz-quartz; Spd-spodumene; Tur-tourmaline.

spodumene + quartz ± muscovite (Fig. 4b). Such replacement also occurs in the rims of coarse-grained spodumene (Fig. 4c). Fluorine-rich apatite, CGM and amblygonite may also occur in symplectites of spodumene + quartz (Fig. 4d). The spodumene crystals show no zoning under optical microscope or in back-scattered electron (BSE) images, but may enclose cassiterite, hydroxylapatite and Fe—Mn oxides in tiny cavities and cracks (Fig. 4e, f, g).

Muscovite has similar textures in rocks of the QM, QAS and QS zones, where it occurs as both primary and secondary phases. Primary muscovite generally appears as large flakes with curved cleavages (Fig. 5a). It is chemically heterogeneous and shows bright and dark domains in high-contrast BSE images (Fig. 5b). Some muscovite flakes display complex core-mantle-rim zoning (Fig. 5c). Lepidolite occurs sporadically as a secondary phase around primary muscovite or along cleavage planes (Fig. 5d). Secondary muscovite is much smaller than primary muscovite and is commonly present in the symplectites of spodumene + quartz (Fig. 5e) or appears as aggregates filling interstitial spaces between albite and quartz (Fig. 5f).

Fine-grained CGM crystals are common in the rocks from the QM, QAS and QS zones. They either occur as inclusions within primary muscovite or fill the interstices between other minerals. The CGM in both occurrences are complexly zoned in high-contrast BSE images with normal (Fig. 6a, b), oscillatory (Fig. 6c) and patchy zoning (Fig. 6e, f). Normally zoned CGM typically has a bright, Ta-rich rim (Fig. 6a, b). Oscillatory zoning in the CGM is commonly overprinted by patchy zoning and chain-like microcavities (Fig. 6d). The CGM with patchy zoning commonly have irregular outlines with obvious embayments (Fig. 6e). In addition, interstitial, relatively uniform grains of CGM are observed in the mineral assemblage of Fe—Mn oxide + hydroxylapatite + quartz (Fig. 6g) or in the symplectites of spodumene + quartz (Fig. 6h).

Accessory apatite is also very common in the rocks from the QM, QAS and QS zones (Fig. 7). Both euhedral to subhedral, F-rich apatite

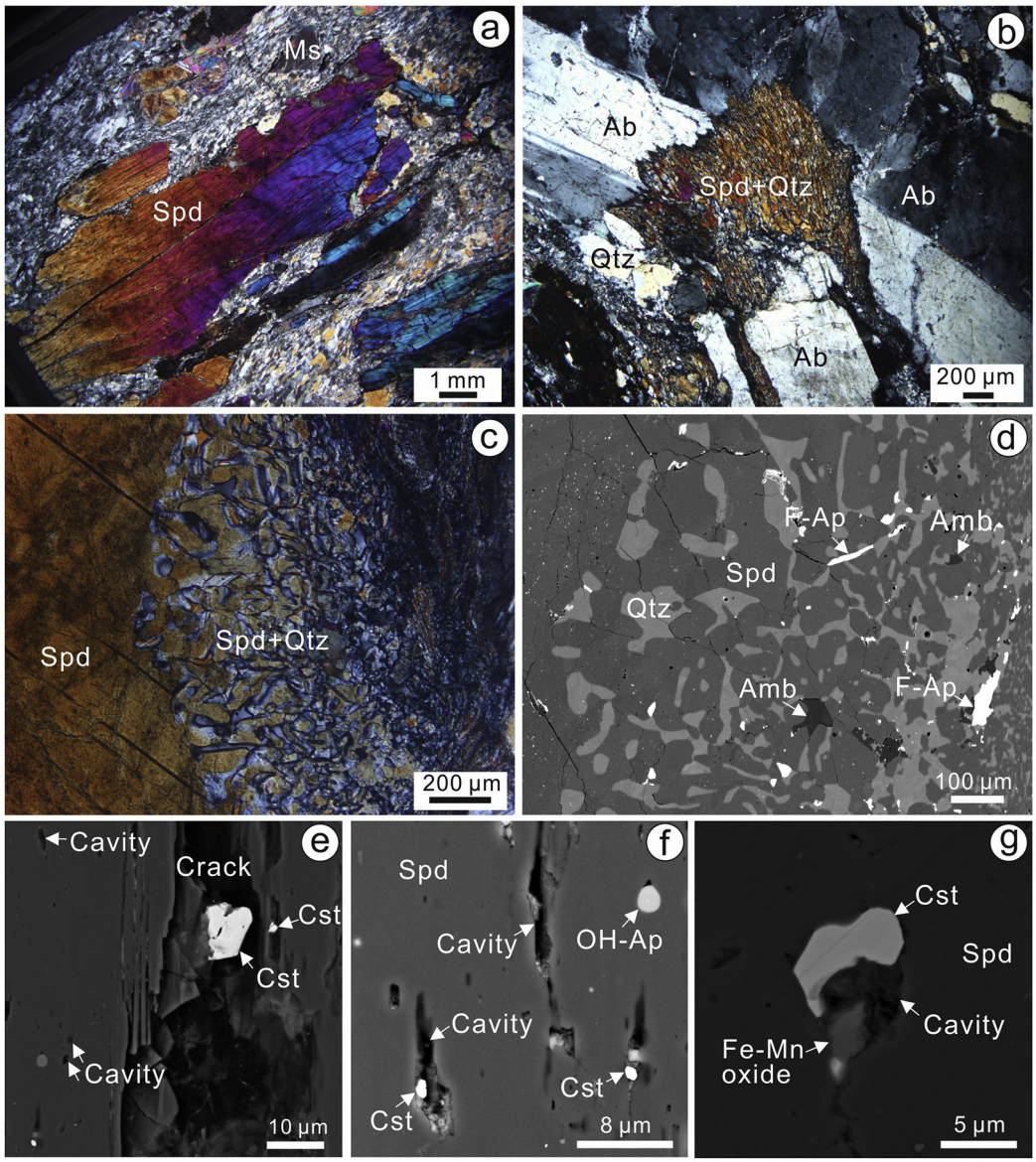

Fig. 4. Photomicrographs and BSE images of spodumene from the Bailongshan pegmatites. (a) Coarse-grained spodumene (Spd) with curved outlines in the quartz-spodumene zone. (b) Symplectite of spodumene + quartz filling the interstices between albite (Ab) and quartz (Qtz) in the quartz-albite-spodumene zone. (c) Partial replacement of a coarse-grained spodumene by spodumene + quartz in the rim. Quartz-spodumene zone. (d) BSE image of the replacive symplectite composed of spodumene + quartz + F-rich apatite (Ap) + amblygonite (Amb) from the quartz-spodumene zone. (e - g) BSE images of micro cracks and cavities in spodumene enclosing cassiterite (Cst), Fe—Mn oxide and hydroxylapatite (OH-Ap). Quartz-spodumene zone.

and secondary hydroxylapatite are observed in thin sections. Overall, F-rich apatite is rare, but in some cases, it is closely associated with CGM where it occupies interstices between muscovite and quartz (Fig. 7a) or occurs in the symplectites of spodumene + quartz (Fig. 4d). In contrast, anhedral hydroxylapatite is commonly present in assemblages of muscovite, spodumene, amblygonite, quartz and CGM (Fig. 7b). It also commonly occupies spaces between twisted cleavage planes of muscovite (Fig. 7c, d), or is intergrown with Fe—Mn oxide and quartz (Fig. 7e, f).

4. Analytical methods

In this study, all samples were prepared as thicker than normal thin sections (>0.08 mm) for quantitative element analysis and elemental mapping. The detailed analytical procedures are as follows.

4.1. Scanning electron microscopy (SEM) and energy dispersive spectrometry (EDS)

Back-scattered electron images were obtained using a Phenom XL SEM at the Key Laboratory of Mineralogy and Metallogeny in the Guangzhou Institute of Geochemistry (GIG), Chinese Academy of Sciences (CAS). EDS analyses were carried out using the same SEM. Operating conditions of 15 kV acceleration voltage, 20 nA beam current, and a working distance of 10 mm were adopted for all EDS analyses.

4.2. Major elements by electron probe micro-analyzer (EPMA)

Major elements of muscovite, CGM and apatite were determined using a JEOL JXA-8230 electron probe micro-analyzer at the same lab in GIGCAS. Operating conditions of 15 kV, 20 nA and a 1 μm beam were adopted for muscovite and CGM analyses, whereas a defocused beam of 3–5 μm was used for apatite. Peak and background counting

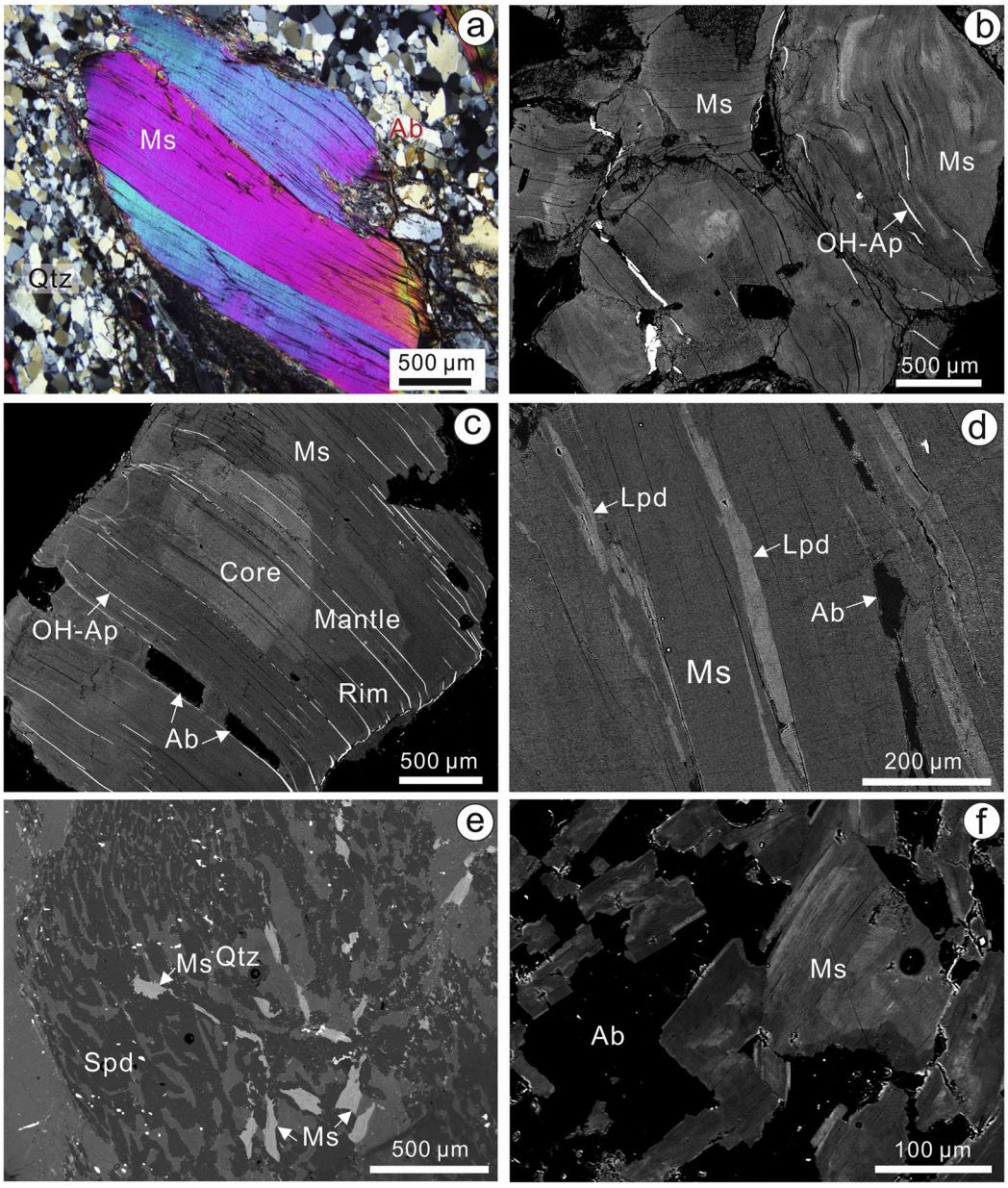

Fig. 5. Photomicrographs and BSE images of muscovite from the Bailongshan pegmatites. (a) Primary muscovite from the quartz-muscovite zone showing twisted cleavages and partial dissolution around the rim. (b) BSE image of primary muscovite from the quartz-albite-spodumene zone showing complex zoning and hydroxylapatite in cleavage planes. (c) BSE image of a primary muscovite from the quartz-albite-spodumene zone showing complex core-mantle-rim texture. (d) BSE image of secondary lepidolite replacing primary muscovite along the cleavage planes of muscovite from the quartz-spodumene zone. (e) BSE image of replacive symplectite of spodumene + quartz + secondary muscovite from the quartz-spodumene zone. (f) BSE image of secondary muscovite aggregates associated with albite from the quartz-albite-spodumene zone. Ab: albite; hydroxylapatite: OH-Ap; Lpd: lepidolite; Ms: muscovite; Qtz: quartz; Spd: spodumene.

times were 10s and 5 s, respectively, for K, Na, F and Cl, 20s and 10s, respectively, for Si, Fe, Mg, Ca, P, Nb, Ta, W, and Sn, 40s and 20s, respectively, for Ti and Mn. Sodium, F and Cl were analyzed first to avoid possible loss during other analyses. The results were reduced using a ZAF correction routine. Standards used for data correction were orthoclase for K, albite for Na, BaF_2 for F, tugtupite for Cl, chrome-diopside for Si and Ca, olivine for Mg, magnetite for Fe, rutile for Ti, rhodonite for Mn, and pure metals for Nb, Ta, W and Sn The results for muscovite, CGM and apatite are shown in Supplementary Tables 1, 2 and 3, respectively.

High-resolution EPMA X-ray elemental intensity mapping for Al, Mn, Fe, Rb and Sn was carried out for a primary muscovite in a sample from the QAS zone. Operating conditions of 20 kV, 200 nA and a 4 μm beam were adopted for mapping. The Al Kα line was analyzed using a TAP crystal and the Mn Kα and Fe Kα lines were analyzed using a LIF crystal. The Rb Lα line was analyzed using a PETJ crystal and the Sn Lα line was analyzed using a PETH crystal. The step size was 4 μm and the dwell time was set to be 100 ms for each point.

4.3. Trace elements by laser ablation inductively coupled-plasma mass spectrometry (LA-ICPMS)

In situ trace element analyses of muscovite were carried out using a laser ablation inductively coupled-plasma mass spectrometer at the same lab in GIGCAS. An Agilent 7900a ICP-MS instrument was coupled to a Resonetic 193 nm ArF excimer laser ablation system. Single spot

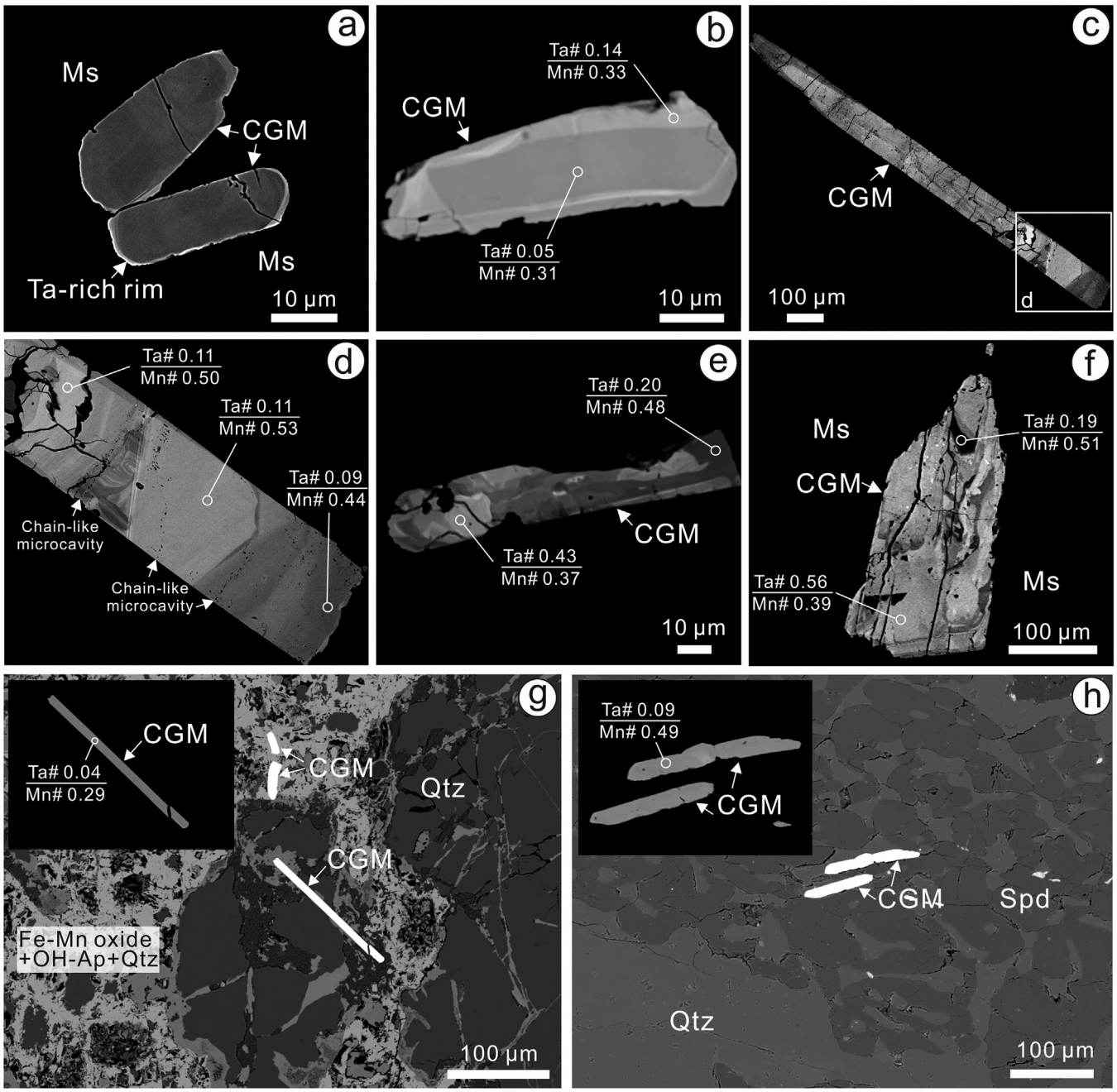

Fig. 6. BSE images of columbite-group minerals (CGM) from the Bailongshan pegmatites. (a - b) Normal zoning of CGM showing a thin, Ta-rich rim. (c) Oscillatory zoning of CGM. (d) Close-up of (c) showing patchy zoning overprinting the oscillatory-zoned crystal. (e - f) Patchy zoning of CGM. (g) CGM in an intergrowth of Fe–Mn oxide + hydroxylapatite (OH-apatite) + quartz (Qtz). (h) CGM in the symplectite of spodumene (Spd) + quartz. (a), (c) and (d) are from the quartz-albite-spodumene zone, (e), (f) and (h) are from the quartz-spodumene zone, (b) and (g) are from the quartz-muscovite zone.

ablation was adopted with a laser beam of 43 μm. Laser energy was 120 mJ and ablation frequency was 6 Hz. Helium was used as a carrier gas and nitrogen was used to enhance sensitivity. Prior to analysis, the LA-ICPMS system was optimized using NIST SRM 610 glass to achieve the maximum signal intensity and low oxide rates. Multiple glass reference materials (BCR-2G, BHVO-2G, BIR-1G and GOR132-G) were used as external calibration references and the Si contents determined by EPMA were used as the internal standard to quantify elemental concentrations. Data reduction was performed using the ICPMSDataCal software (version 10.2) (Lin et al., 2016; Liu et al., 2008). The analytical uncertainties are 5–10% for trace elements and generally better than 5% for major elements. The full dataset of muscovite is listed in Supplementary Table 4. The measured trace element concentrations of NIST SRM 610, BIR-1G, GOR132-G, BHVO-2G and BCR-2G glasses and their recommended values are listed in Supplementary Table 5.

4.4. LA-ICPMS mapping

LA-ICPMS mapping of a primary muscovite in a sample from the QS zone was performed at the Ore Deposit and Exploration Centre (ODEC), School of Resources and Environmental Engineering, Hefei University of Technology. A laser ablation system (PhotonMachines Analyte HE with

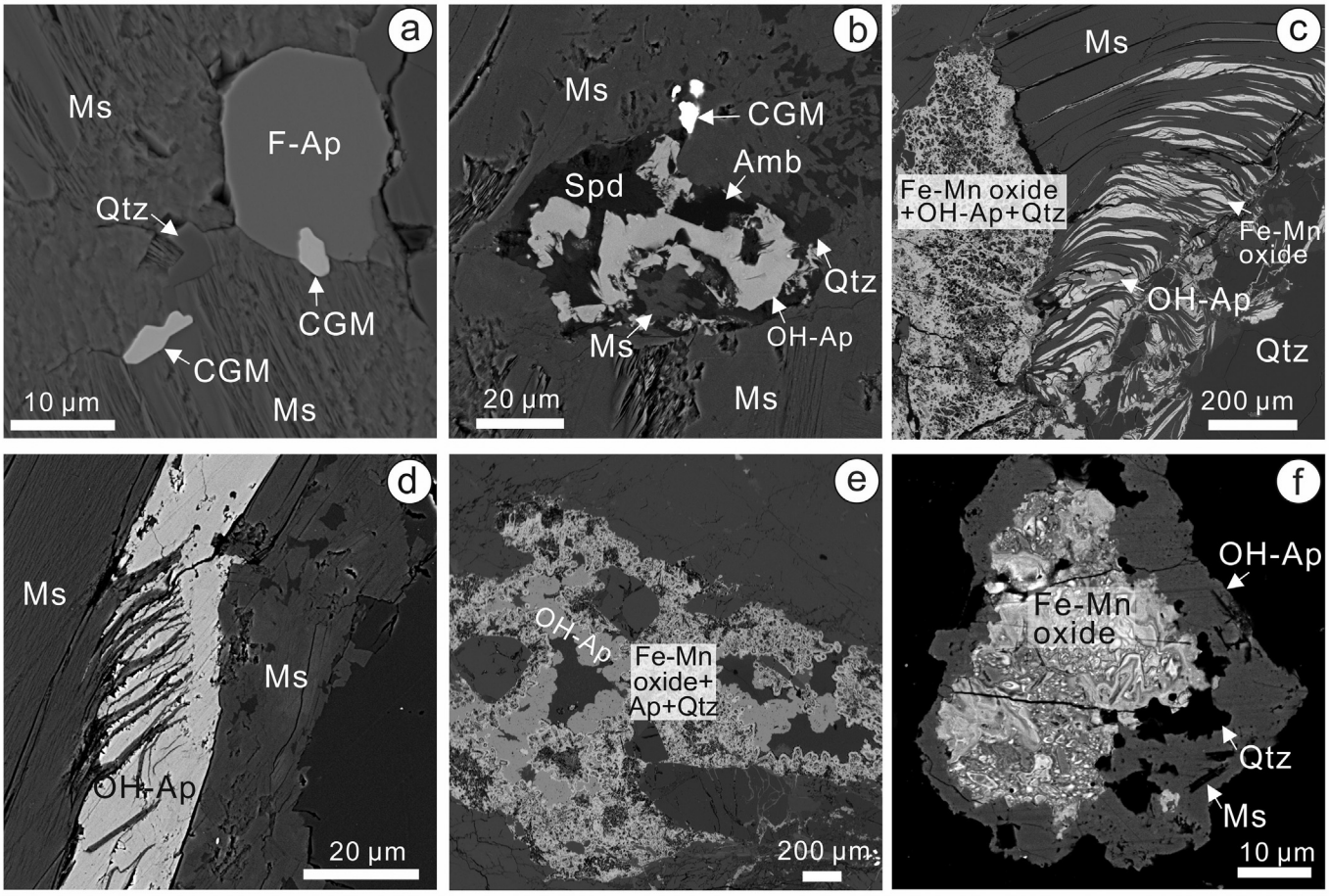

Fig. 7. BSE images of apatite from the Bailongshan pegmatites. (a) Subhedral, F-rich apatite associated with CGM from the quartz-albite-spodumene zone. (b) Mineral clusters of spodumene (Spd) + hydroxylapatite (OH-Ap) + muscovite (Ms) + quartz (Qtz) + CGM + amblygonite (Amb) from the quartz-spodumene zone. (c - d) Anhedral hydroxylapatite with Fe—Mn oxide filling the twisted cleavage planes of muscovite from the quartz-muscovite zone. (e - f) Intergrowths of hydroxylapatite + Fe—Mn oxide + quartz + muscovite from the quartz-muscovite zone.

193-nm ArF Excimer) was installed to the Agilent 7900 quadrupole-based inductively coupled plasma-mass spectrometer (Ning et al., 2017). The Analyte HE utilizes a two-volume ablation cell designed by Laurin Technic Pty. Ablation was performed in an atmosphere of UHP He (0.9 L/min), and upon exiting the cell the aerosol was mixed with Ar (0.87 L/min) immediately via a T-connector before entering the ICP. In addition, for high resolution profiling, the signal-smoothing device used for routine analysis was removed to acquire an almost instantaneous response time. The ICP-MS system was optimized before sample mapping to maximize sensitivity on isotopes of the mass range of interest, while keeping production of molecular oxide species (i.e., $^{232}Th^{16}O/^{232}Th$) as low as possible, usually <0.3%. Elemental maps were created by ablating sets of parallel line rasters in a grid across the sample. The laser beam size was set to be 20 μm and the scan speed was 20 μm/s. A laser repetition of 10 Hz was selected at a constant energy output of 50 mJ, resulting in an energy density of ~3 J/cm^2 at the target. A 20-s background count was acquired at the start of scanning, and to allow for cell wash-out, gas stabilization, and computer processing, and a delay of 20s was set after ablation. Reference material NIST 610 was analyzed at the start and end of each mapping session for data calibration. Images were compiled and processed using the program LIMS (Wang et al., 2017b; Xiao et al., 2018). For each raster and every element, the average background was subtracted from its corresponding raster, and the rasters were compiled into a 2-D image displaying combined background/drift-corrected intensity for each element (Wang et al., 2017b).

5. Results

5.1. Major and trace element compositions of muscovite

Primary muscovite from rocks of the QAS and QS zones has similar compositions, and contains 0.66 to 1.20 wt% FeO_t and 1.93 to 1.98 Al^{vi} (Fig. 8a; Supplementary Table 1), whereas that from rocks of the QM zone contains 1.18 to 2.06 wt% FeO_t and 1.89 to 1.94 Al^{iv} (Fig. 8a). Muscovite in all three zones has MnO and TiO_2 < 0.1 wt%, and F and Cl contents below detection limits. In contrast, secondary muscovite from the QAS zone shows large variations of FeO_t and Al^{iv} (Fig. 8a).

Primary muscovite from rocks of the QM zone has K/Rb varying from 26.0 to 19.3, whereas that from the QAS and QS zones has lower ratios with K/Rb varying between 19.3 and 7.8 (Supplementary Table 4). The K/Rb ratios of primary muscovite decrease from the QM zone through the QAS zone to the QS zone (Fig. 9). The decreasing trend of K/Rb is accompanied by slight increases in Li and Be, remarkable increases in B, Cs, Rb and Ta/Nb, and a decrease of Nb (Fig. 9). Primary muscovite from rocks of three zones has Ta/Nb ratios varying from 0.05 to 0.31, 0.07 to 0.12 and 0.09 to 1.27, respectively (Supplementary Table 4). Overall, primary muscovite from the QM zone has higher Nb and lower Ta/Nb than that in the QAS and QS zones (Fig. 9e, f).

Secondary muscovite from rocks of the QAS zone has highly variable Li, Be, B, Cs and Nb (Fig. 9; Supplementary Table 4). It is relatively enriched in Li, Be, B and Cs and very depleted in Nb compared with

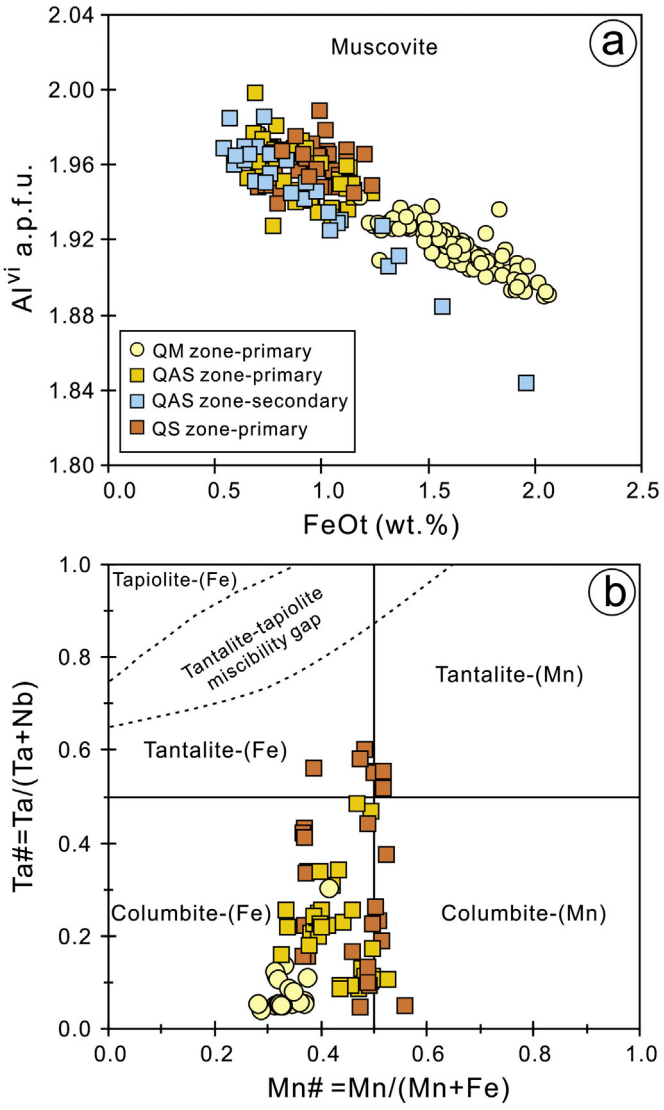

Fig. 8. Binary plots of FeOt versus Al^{vi} contents in muscovite (a) and Mn# versus Ta# of CGM (b) from the Bailongshan pegmatites.

primary muscovite (Fig. 9). Secondary muscovite also has variable K/Rb and Ta/Nb ratios ranging from 20.3 to 10.5 and from 0.13 to 0.84, respectively (Supplementary Table 4).

Core-to-rim profiles for primary muscovite reveal significant trace element variations depending on whether the muscovite has hydroxylapatite or lepidolite along the cleavage planes (Fig. 10). The profile for muscovite with hydroxylapatite shows a gradual increase in B from the core to the mantle and then a pronounced drop in the rim; the same profile shows gradual decreases in Rb and Cs, although Rb drops abruptly to lower values in the rim (Fig. 10b, c, d). The K/Rb ratio increases gradually from core to mantle, and then increases abruptly in the rim (Fig. 10e). The Ta/Nb ratios show little variation through the profile (Fig. 10f).

The profile for muscovite with lepidolite shows decreasing B in the core, followed by a steady rise from mantle to rim (Fig. 10h), whereas Rb decreases rapidly in the core, rises in the mantle and then falls somewhat in the rim (Fig. 10j), and Cs shows a generally similar pattern. The K/Rb ratio is generally flat except for a small increase in the core and rim, whereas the Ta/Nb ratio is constant within each of the three zones but is notably higher in the mantle than either the core or rim (Fig. 10h,i).

5.2. Elemental distribution maps of muscovite

The X-ray element mapping for a primary muscovite from the QAS zone shows that the muscovite is complexly zoned with highly variable Al, Fe, Mn, Rb and Sn contents (Fig. 11). The core has lower Al and higher Fe, Mn, Rb and Sn than either the mantle or rim. The mantle and rim have similar Al, Fe, Mn and Sn, however, the rim has lower Rb than the mantle (Fig. 11).

The high-resolution trace element mapping of a partially dissolved, primary muscovite from the QS zone reveals a heterogeneous distribution of Li, Rb, Cs, Ta, Fe, Ti, Mn, Nb and Sn (Fig. 12). The Cs and Ta within the muscovite show three distinct domains (Fig. 12i, n); Domain 1 in the center has high Cs, Ta, Li, Fe, Ti, Mn and Nb and low Sn; Domain 2 on the right side of Domain 1 has low Cs, Ta, Li, Ti and high Sn, whereas Domain 3 at the two corners of the grain has very high Cs, Ta and Li and low Rb and Nb (Fig. 12).

5.3. Major element compositions of columbite-group minerals

The CGM in the samples from the QAS and QS zones have similar compositions. They have higher and more variable Ta#s [Ta/(Ta + Nb)] and Mn#s [Mn/(Mn + Fe)] than those from the QM zone (Fig. 8b; Supplementary Table 2).

In CGM with normal zoning the Ta# increases from 0.05 in the core to 0.14 in the rim with a nearly constant Mn# (Fig. 6b). Grains of CGM with oscillatory and patchy zoning have high Ta# (0.11) and Mn# (0.53) in the primary domain and low Ta#s (0.09) and Mn#s (0.44) in the replaced domain (Fig. 6d). In particular, CGM grains with patchy zoning have highly variable Ta#s (0.20–0.43) and Mn#s (0.48–0.37) within a single grain (Fig. 6e, f). Uniform CGM grains with interstitial Fe—Mn oxides and hydroxylapatite or in the symplectites have low Ta#s (0.04 to 0.09) and variable Mn#s (0.29 to 0.49) (Fig. 6g, h).

5.4. Major element compositions of apatite

Apatite from the QM, QAS and QS zones varies from fluorapatite to hydroxylapatite (Supplementary Table 3). Euhedral, F-rich apatite grains scattered in the interstitial spaces contain 1.66 to 3.72 wt% F and 0.22 to 1.67 wt% MnO (Supplementary Table 3). Euhedral to subhedral grains filling microcracks in spodumene contain 1.43 to 3.84 wt% F and 0.29 to 1.11 wt% MnO. Anhedral hydroxylapatite that fills the twisted cleavages of muscovite or coexists with interstitial Fe—Mn oxides contains 0.12 to 0.78 wt% MnO and has F contents below the detection limit of EPMA.

6. Discussion

6.1. Crystallization of muscovite and columbite-group minerals

Primary muscovite of the Bailongshan pegmatites overall shows a gradual decrease in K/Rb ratios and an increase in Ta/Nb from the QM zone through the QAS zone to the QS zone (Fig. 9 and Supplementary Table 4). K/Rb ratios of muscovite are generally considered to be geochemical indicators for pegmatite evolution. Because Rb is incompatible in K-feldspar and less compatible than K in muscovite (Icenhower and

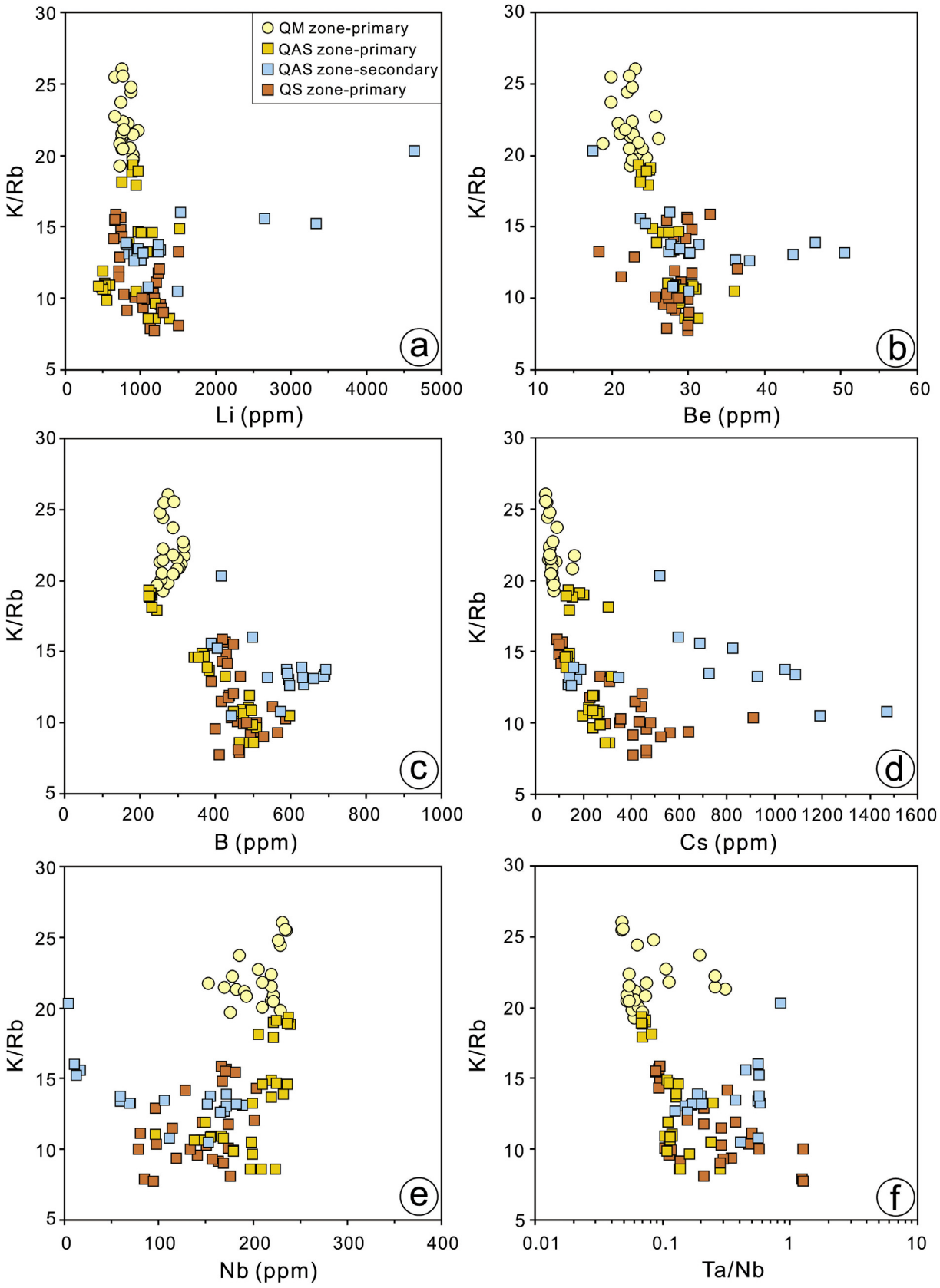

Fig. 9. Binary plots of K/Rb ratios versus Li (a), Be (b), B(c), Cs (d), Nb (e), and Ta/Nb ratio (f) of muscovite from the Bailongshan pegmatites.

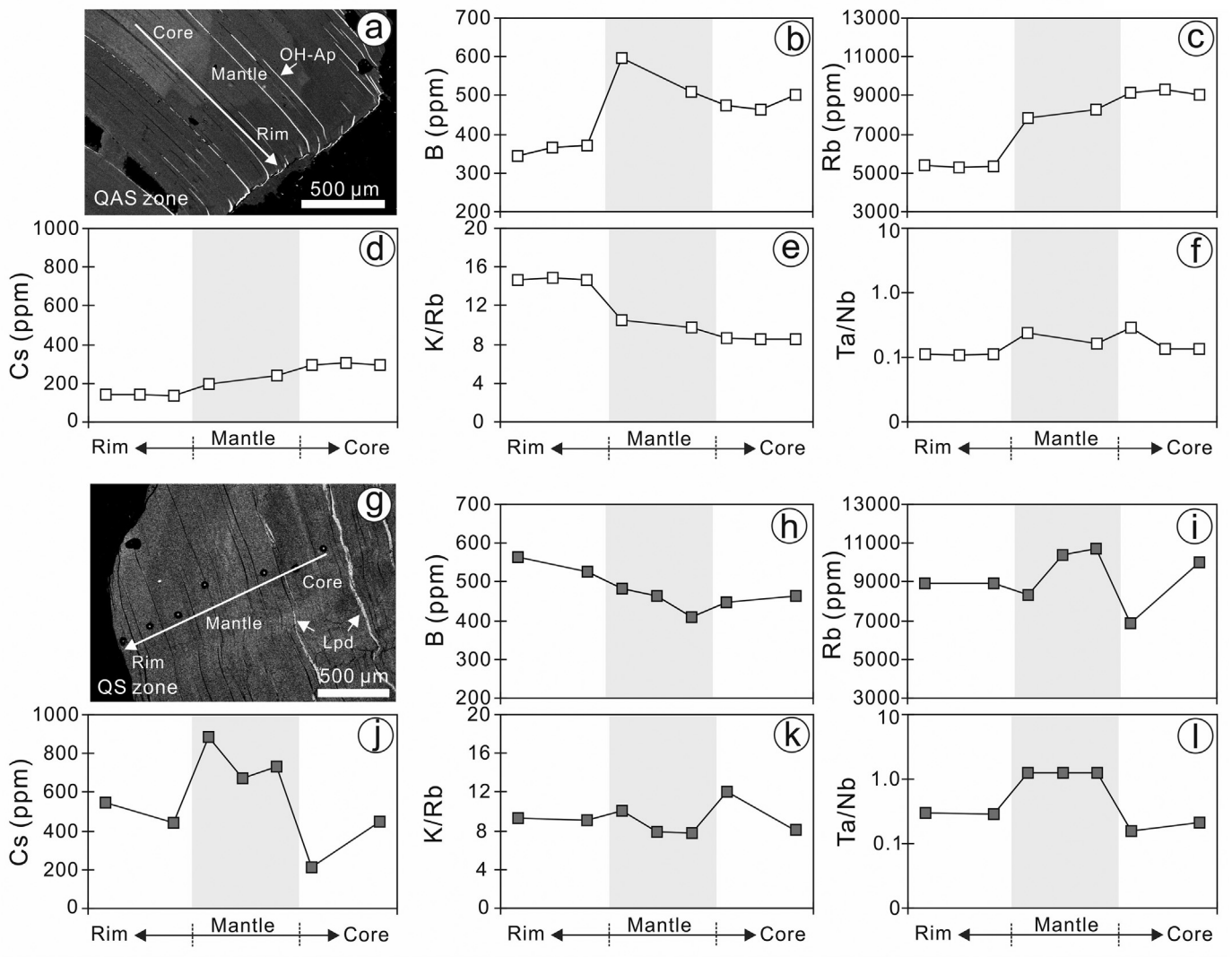

Fig. 10. BSE images and core-to-rim profiles of major and trace element compositions of primary muscovite from rocks of the quartz-albite-spodumene zone (a-f) and quartz-spodumene zone (g-l). Note the secondary hydroxylapatite (OH-Ap) and lepidolite (Lpd) in the cleavage planes of muscovite.

London, 1995, 1996), crystallization of K-feldspar and muscovite would lead to the evolved melts being progressively enriched in Rb, resulting in decreasing K/Rb ratios. Muscovite crystallized from late-stage, evolved melts would then have lower K/Rb ratios and higher Rb concentrations than early crystallized muscovite (Černý et al., 1985a; Hulsbosch et al., 2014).

Experimental results demonstrate that the solubility of columbite is lower than tantanlite in granitic melts and the solubility of the two minerals would dramatically increase with increasing alkalis, F and Li contents of the melts (Chevychelov et al., 2010; Linnen, 1998; Linnen and Keppler, 1997). If columbite crystallizes early, the evolved melt would be progressively depleted in Nb, resulting in high Ta/Nb ratios. Muscovite crystallized from the evolved melts would then also have higher Ta/Nb ratios than early crystallized muscovite. In the Bailongshan pegmatites, primary muscovite from rocks of the QM zone has the highest K/Rb ratio (26.0) and lowest Ta/Nb ratio (0.05), whereas that from the QS zone has the lowest K/Rb ratio (7.8) and highest Ta/Nb ratio (1.27) (Fig. 9), indicating that the compositions of primary muscovite from the QM zone to the QS zone overall record a progressive crystallization of pegmatitic magma.

The CGM from rocks of the QM to QS zones show an increase of Mn#s from ~0.3 to 0.5, with highly variable Ta#s within each zone (Fig. 8b), a trend consistent with magmatic fractionation, i.e., early crystallization of ferrocolumbite ($FeNb_2O_6$) relative to manganotantalite ($MnTa_2O_6$) (Anderson et al., 2013; Černý et al., 1985b). The large variation of Ta#s for CGM within each zone indicates that the CGM likely experienced multiple stages of crystallization, an interpretation supported by the complex zoning patterns of the grains (Fig. 6). Normal and oscillatory zoning of the CGM (Fig. 6a, b, c) are generally considered to be magmatic in origin, whereas patchy zoning and corroded and embayed textures (Fig. 6d, e, f) indicate fluid/melt-induced partial dissolution (*c. f.*, Anderson et al., 2013).

Core-to-rim profiles of the CGM grains document highly variable Ta#s (Fig. 13). The cores are characterized by relatively low Ta#,

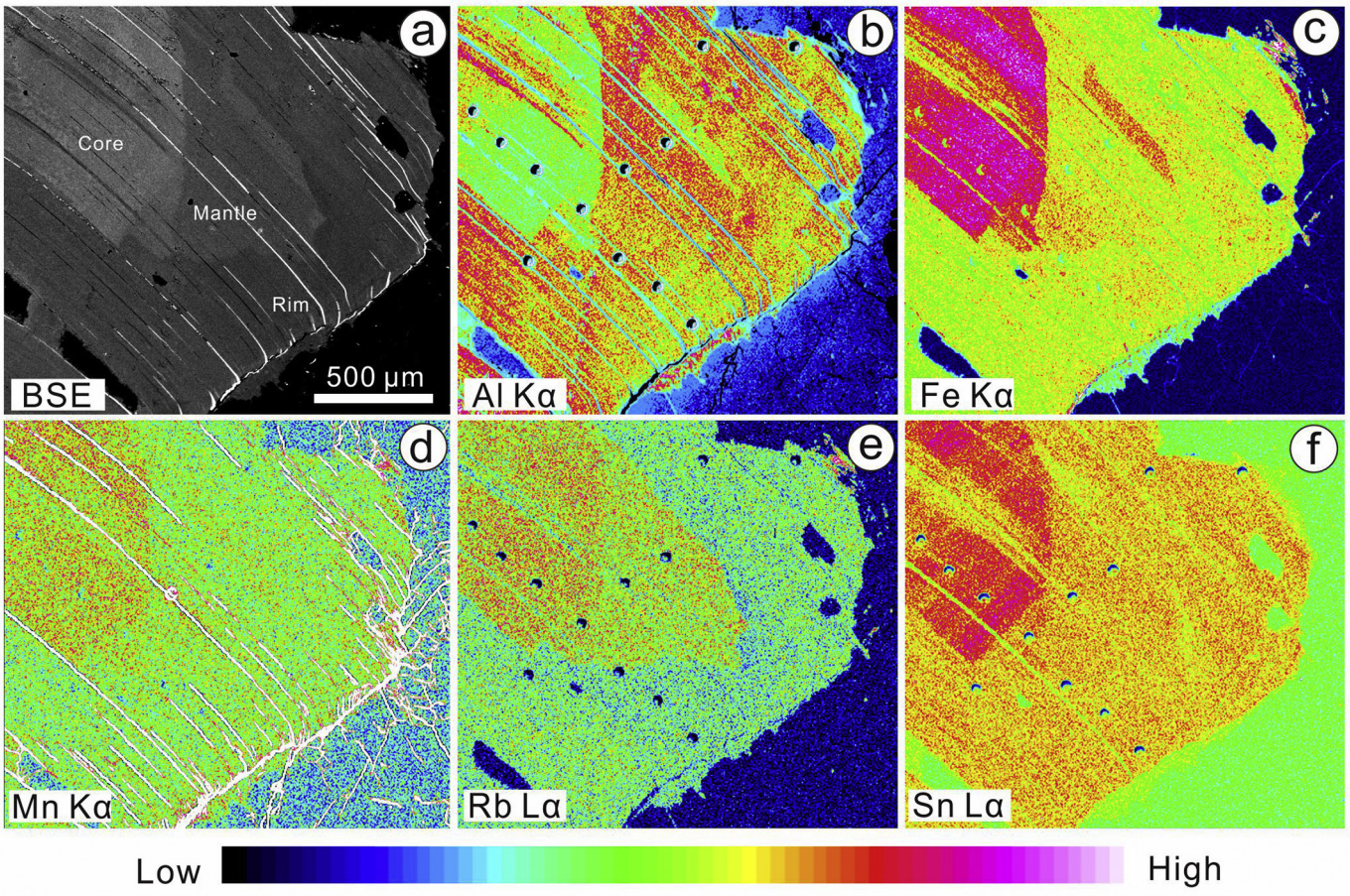

Fig. 11. BSE image (a) and elemental distribution maps of Al (b), Fe (c), Mn (d), Rb (e) and Sn (f) of a primary muscovite grain from rock of the quartz-albite-spodumene zone.

which is followed by an abrupt increase in the mantle, and then a decrease in the rim (Fig. 13). Such variations of Ta#s in the CGM of the Bailongshan pegmatites are similar to that for the CGM from the Moose II pegmatite in Canada, which is interpreted as reflecting three stages of growth, beginning with Nb- and Ta-rich magmatic grains followed by Nb-rich CGM from late-stage fluids (Anderson et al., 2013). We note that the CGM intergrown with Fe—Mn oxide + hydroxylapatite + quartz or in symplectites with spodumene + quartz have very low Ta#s of 0.04 to 0.09 (Fig. 6g, h), indicating precipitation of CGM from late-stage fluids.

Secondary muscovite in the symplectites contains extremely low Nb (Fig. 9e), which may be due to the depletion of Nb in the late-stage fluids after the crystallization of Nb-rich CGM. Therefore, we consider that both muscovite and CGM from the Bailongshan pegmatites record a progressive crystallization process from magma to late-stage fluid.

6.2. Overprinting of primary muscovite by fluid/melt metasomatism

Overprinted fluid/melt metasomatism in granitic pegmatites can lead to the crystallization of secondary muscovite, such as that in the Moose II pegmatite and the Tanco pegmatite in Canada (Anderson et al., 2013; Van Lichtervelde et al., 2008). In addition to secondary muscovite, elongated hydroxylapatite and lepidolite commonly either grow along cleavage planes or occur around the rims of primary muscovite in the Bailongshan pegmatites (Fig. 5c, d). In our samples, hydroxylapatite has F contents below the detection limit of EPMA, whereas lepidolite contains up to 5.95 wt% F (Supplementary Table 1). Therefore, the coexistence of hydroxylapatite and lepidolite in primary muscovite indicates that these secondary phases in the cleavage planes and rims may have crystallized from different late-stage fluids/melts.

Muscovite in the Bailongshan pegmatites with hydroxylapatite in cleavage planes has lower B, Rb, Cs, Sn and higher K/Rb ratios in the rims than the cores (Figs. 10b-e and 11). We attribute this to fluid metasomatism that released elements such as B, Rb, Cs and Sn from primary muscovite, thus enriching the fluids in these elements, producing the higher K/Rb ratios of primary muscovite. Given that hydroxylapatite contains very little F and Cl, the fluids were likely poor in these elements. On the other hand, the common presence of intergrown Fe—Mn oxides + hydroxylapatite + quartz (Fig. 7) indicates that the fluids were enriched in P, Fe and Mn. The presence of cassiterite in cleavage planes of muscovite and in microcavities in spodumene (Fig. 4e-g) indicates that the fluids were also enriched in Sn. Spodumene from rocks of the QAS and QS zones commonly have corroded rims and symplectites of spodumene + quartz (Fig. 4a, b), indicating that significant amounts of Li may have been released from spodumene into the fluid. Therefore, any secondary muscovite crystallized from late-stage fluids could be enriched in Li, Be, B, Rb, Sn and Cs (Fig. 9).

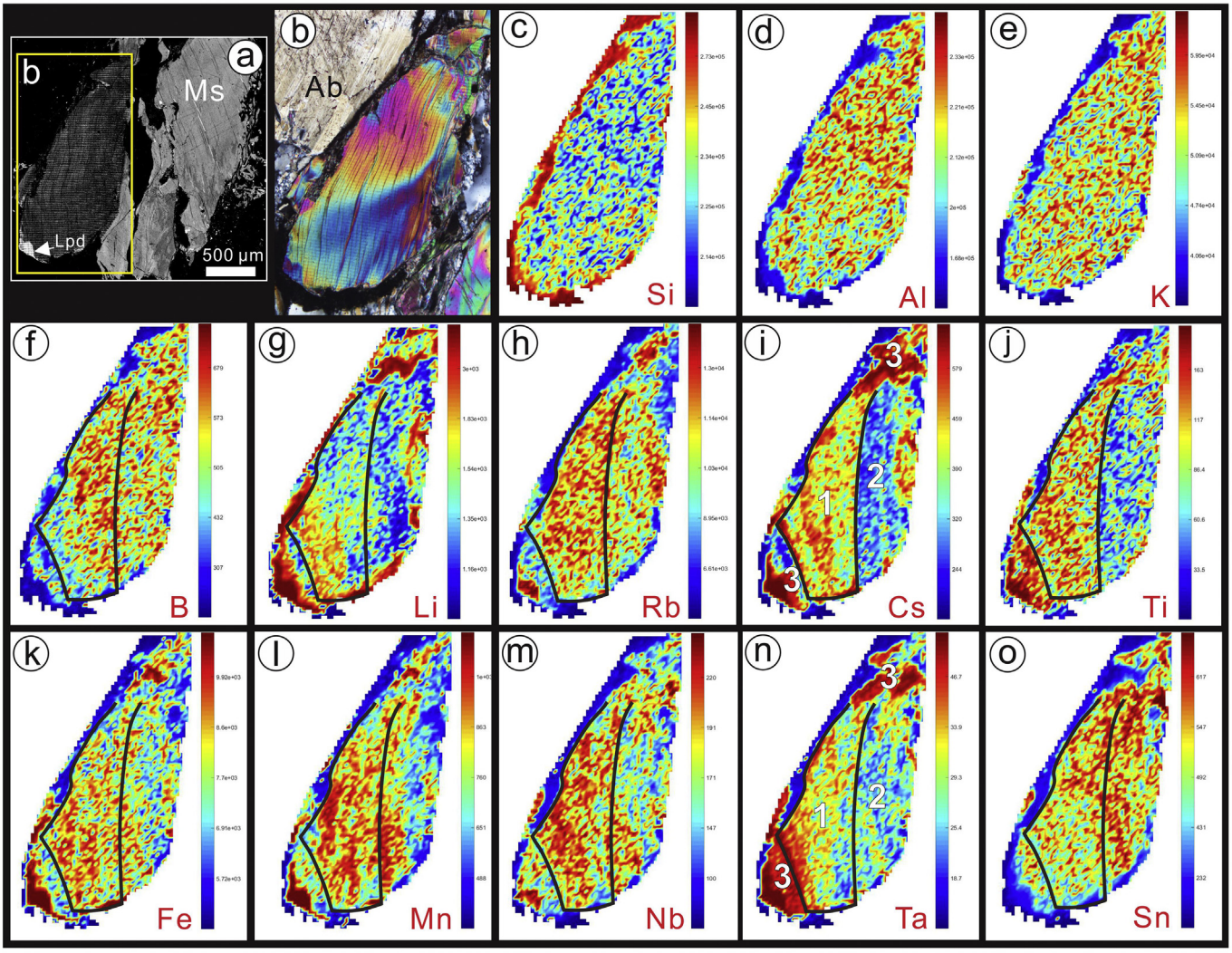

Fig. 12. BSE image (a), photomicrograph (b) and trace element distribution maps (c-o) of a primary muscovite from rock of the quartz-spodumene zone. Note that three domains with contrasting Cs and Ta concentrations are marked as 1, 2 and 3, respectively. The small bright domain at the lower left corner of the muscovite shown in (a) is lepidolite (Lpd).

Trace element mapping of primary muscovite with lepidolite in its rim shows that the parts adjacent to the lepidolite are highly enriched in Ta, Cs and Li and depleted in Nb, Rb, B and Sn (see Domain 3 in Fig. 12). The profile of primary muscovite with lepidolite in cleavage planes also shows remarkable increases in Cs and Ta/Nb ratios in the mantle area with nearly constant K/Rb throughout the profile (Fig. 10i-l). These features are distinctly different from those of muscovite that experienced fluid metasomatism (Fig. 10b-f). Nb and Ta are nearly insoluble in hydrothermal fluids, and the transport of these elements is possible only in F-rich fluids (Chevychelov et al., 2005, 2010; Zaraisky et al., 2010). Therefore, F-poor fluid metasomatism would hardly remobilize Ta and Nb of primary muscovite. However, Ta is highly soluble relative to Nb in granitic melts, particularly in Li- or F-rich melts (Linnen, 1998; Linnen and Keppler, 1997). Therefore, we consider the local enrichment of Li, Cs and Ta in the rims of primary muscovite with high Ta/Nb ratios to have been the result of melt metasomatism. Such a F-Li-Cs-Ta-rich melt may have formed during the late-stage evolution of the pegmatitic magma.

6.3. Processes related to evolution of the Bailongshan pegmatites

Primary muscovite from rocks of the QS zone has three trace element domains. Domain 1 in the central part of the grain contains higher Cs and Ta concentrations than Domain 2, which lies in the margin (Fig. 12i, n). Because Domain 2 has higher Sn and lower Cs than Domain 1 (Fig. 12i, o), it cannot have been formed by fluid metasomatism. Metasomatism would have lowered both Sn and Cs in the primary muscovite (Figs. 10d and 11f). Thus, the higher Sn and lower Cs and Ta in Domain 2 are attributed to growth of the primary grain.

Experimental results and fluid/melt inclusion studies demonstrate that melt/fluid immiscibility can occur during the last stage of pegmatite evolution, producing a silicate melt, a hydrosaline melt/fluid phase and a hydrothermal fluid (or vapor), which may result in a three-phase equilibrium at the magmatic-hydrothermal transition stage (Kamenetsky et al., 2004; Thomas and Davidson, 2016; Veksler, 2004 and references therein). During melt/fluid immiscibility, Cs and Ta would be preferentially partitioned into the silicate melt, whereas Be,

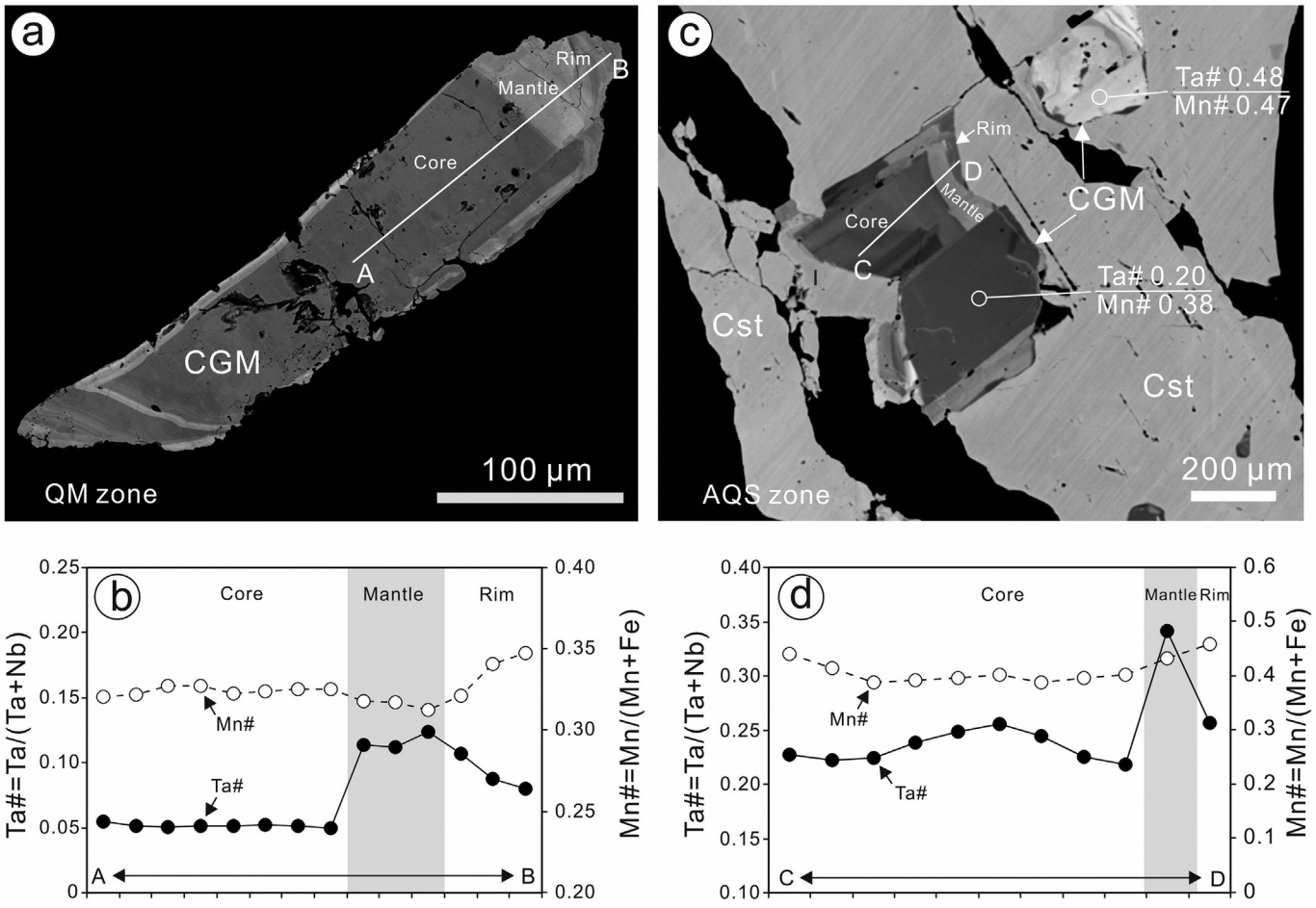

Fig. 13. Core-to-rim profiles of Ta# and Mn# for CGM from rocks of the quartz-muscovite zone (a-b) and the quartz-albite-spodumene zone (c-d). Note that CGM enclosed within cassiterite (Cst) shown in (b) has variable Ta# and Mn#.

B, Cl, Na, P, Fe, Mn, Sn, Zr and Nb would be preferentially partitioned into the hydrosaline melt/fluid (Rickers et al., 2006; Thomas et al., 2000, 2003; Veksler, 2004). Both melts could be progressively enriched in F with fractional crystallization (Kaeter et al., 2018). An apparent loss of Cs in muscovite of the Leinster pegmatites in SE Ireland is attributed to a shift of crystallization from the silicate melt to the hydrosaline melt/fluid (Kaeter et al., 2018). Likewise, Domain 2 in primary muscovite may have crystallized from a hydrosaline melt/fluid so that it is enriched in Sn but poor in Cs and Ta. On the other hand, fractionated silicate melt with high Ta/Nb and Cs/Rb may interact with primary muscovite, leading to local enrichment of Ta and Cs relative to Nb and Rb in Domain 3 (Fig. 12).

Boron is considered to be an important fluxing element that exerts a significant control on pegmatite evolution and melt/fluid immiscibility (Thomas et al., 2003). Both primary and secondary muscovite from the Bailongshan pegmatites contain >200 ppm B (Supplementary Table 4), which is much higher than values for muscovite from LCT-type pegmatites elsewhere, such as the Leinster pegmatite in SE Ireland, and the Tanco and Moose II pegmatites in Canada (Anderson et al., 2013; Kaeter et al., 2018; Van Lichtervelde et al., 2008) (Fig. 14). On plots of B versus rare elements, muscovite from the Bailongshan pegmatites shows positive correlations between B and Rb, Cs and Ta/Nb ratios and a weak positive correlation between B and Li (Fig. 14), indicating that the Bailongshan pegmatites likely formed from an initially B-rich melt. The involvement of B in the system may have facilitated enrichment and fractionation of rare elements during evolution of the pegmatites.

7. Conclusions

Muscovite and CGM in rocks of the QM, QAS and QS zones of the Bailiongshan pegmatites formed under complex magmatic-hydrothermal processes. Primary muscovite from the QM to QS zones overall shows a gradual decrease of K/Rb and increase of Ta/Nb ratios, indicating progressive fractionation of the parental magmas. The CGM grains display complex zoning patterns and have Mn#s increasing from the QM zone to QS zone with variable Ta#s within each zone. The CGM formed in a three-stage growth process, i.e., Nb-rich CGM and Ta-rich CGM formed in the initial magmatic stage and Nb-rich CGM later formed again in the hydrothermal stage. Metasomatism by F-poor fluids released Fe, Mn, B, Rb, Cs and Sn from the primary muscovite, leading to complex zoning patterns in the muscovite and to crystallization of secondary hydroxylapatite in cleavage planes of the muscovite. Metasomatism by the F-Li-Cs-Ta-rich melt produced local

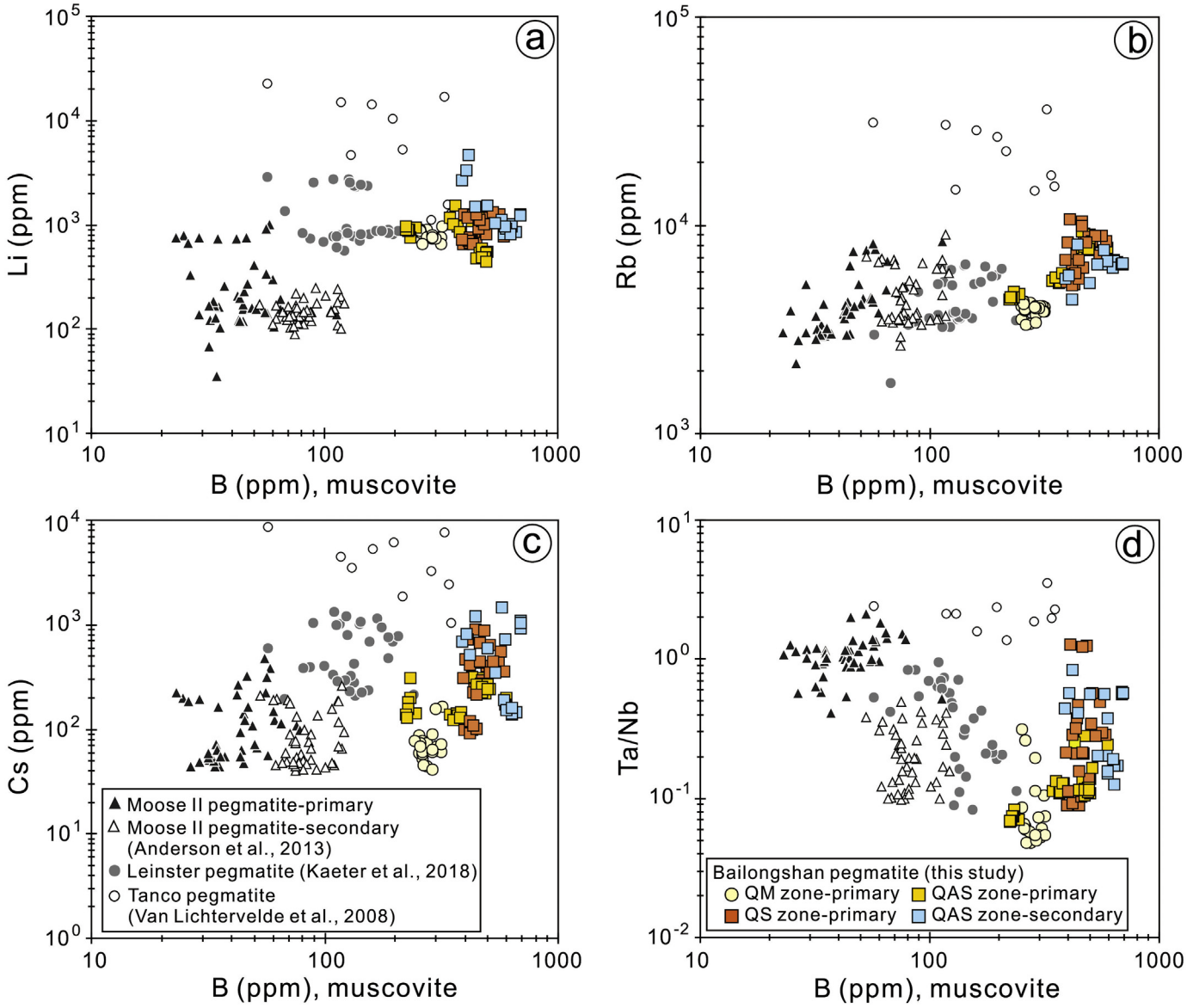

Fig. 14. Binary plots of boron versus Li (a), Rb (b), Cs (c), and Ta/Nb (d) of muscovite from the Bailongshan pegmatites. Compositions of muscovite from the LCT-type pegmatites elsewhere in the world are shown for comparison.

enrichment of Li, Cs and Ta and secondary lepidolite in the cleavage planes and rims of the primary muscovite. The parental melt of the Bailongshan pegmatites was likely rich in B resulting in higher B in the primary muscovite than that found in other LCT-type pegmatites elsewhere in the world.

Supplementary data to this article can be found online at https://doi.org/10.1016/j.lithos.2020.105507.

Declaration of Competing Interest

The authors declare that they have no known competing financial interests or personal relationships that could have appeared to influence the work reported in this paper.

Acknowledgements

This study was financially supported by the Second Tibetan Plateau Scientific Expedition and Research Program (2019QZKK0802), the Strategic Priority Research Program (B) of the Chinese Academy of Sciences (XDB18000000), and the Youth Innovation Promotion Association CAS (2018388). Yuhang Jiang is thanked for helping with sample collecting in the field and Linya Ma, Dan Wu and Fangyue Wang are thanked for providing assistance during SEM-EDS and LA-ICPMS spot analysis and LA-ICPMS mapping. Paul Robinson kindly helped polishing the English of revised manuscript. We also thank Miguel Ángel Galliski, one anonymous reviewer and guest editor, Yigang Xu, for their constructive comments on the manuscript.

References

Anderson, M., Lentz, D., McFarlane, C., Falck, H., 2013. A geological, geochemical and textural study of an LCT pegmatite: Implications for the magmatic versus metasomatic origin of Nb-Ta mineralization in the Moose II pegmatite, NWT, Canada. J. Geosci. 58, 299–320.

Ballouard, C., Poujol, M., Boulvais, P., Branquet, Y., Tartese, R., Vigneresse, J.L., 2016. Nb-Ta fractionation in peraluminous granites: a marker of the magmatic- hydrothermal transition. Geology 44 (3), 231–234.

Černý, P., Meintzer, R.E., Anderson, A.J., 1985a. Extreme fractionation in rare-element granitic pegmatites; selected examples of data and mechanisms. Can. Mineral. 23 (3), 381–421.

Černý, P., Roberts, W.L., Ercit, T.S., Chapman, R., 1985b. Wodginite and associated oxide minerals from the Peerless pegmatite, Pennington County, South Dakota. Am. Mineral. 70 (9–10), 1044–1049.
Černý, Peter, Blevin, P.L., Cuney, M., London, D., 2005. Granite-related ore deposits. Econ. Geol. 100, 337–370.
Chevychelov, V., Zaraisky, G.P., Borisovskiy, S., Borkov, D.A., 2005. Effect of melt composition and temperature on the partitioning of Ta, Nb, Mn, and F between granitic (alkaline) melt and fluorine-bearing aqueous fluid: Fractionation of Ta and Nb and conditions of ore formation in rare-metal granites. Petrology 13, 339–357.
Chevychelov, V.Y., Borodulin, G.P., Zaraisky, G.P., 2010. Solubility of columbite, $(Mn, Fe)(Nb, Ta)_2O_6$, in granitoid and alkaline melts at 650-850°C and 30-400 MPa: an experimental investigation. Geochem. Int. 48, 456–464.
Halter, W.E., Webster, J.D., 2004. The magmatic to hydrothermal transition and its bearing on ore-forming systems. Chem. Geol. 210, 1–6.
Hulsbosch, N., Hertogen, J., Dewaele, S., André, L., Muchez, P., 2014. Alkali metal and rare earth element evolution of rock-forming minerals from the Gatumba area pegmatites (Rwanda): Quantitative assessment of crystal-melt fractionation in the regional zonation of pegmatite groups. Geochim. Cosmochim. Acta 132, 349–374.
Icenhower, J., London, D., 1995. An experimental study of element partitioning among biotite, muscovite, and coexisting peraluminous silicic melt at 200 MPa (H_2O). Am. Mineral. 80 (11−12), 1229–1251.
Icenhower, J., London, D., 1996. Experimental partitioning of Rb, Cs, Sr, and Ba between alkali feldspar and peraluminous melt. Am. Mineral. 81 (5–6), 719–734.
Jolliff, B.L., Papike, J.J., Shearer, C.K., 1987. Fractionation trends in mica and tourmaline as indicators of pegmatite internal evolution: Bob Ingersoll pegmatite, Black Hills, South Dakota. Geochim. Cosmochim. Acta 51, 519–534.
Kaeter, D., Barros, R., Menuge, J.F., Chew, D.M., 2018. The magmatic–hydrothermal transition in rare-element pegmatites from Southeast Ireland: LA-ICP-MS chemical mapping of muscovite and columbite-tantalite. Geochim. Cosmochim. Acta 240, 98–130.
Kamenetsky, V.S., Naumov, V.B., Davidson, P., Van Achterbergh, E., Ryan, C.G., 2004. Immiscibility between silicate magmas and aqueous fluids: a melt inclusion pursuit into the magmatic-hydrothermal transition in the Omsukchan Granite (NE Russia). Chem. Geol. 210 (1–4), 73–90.
Lin, J., Liu, Y.S., Yang, Y.H., Hu, Z.C., 2016. Calibration and correction of LA-ICP-MS and LA-MC-ICP-MS analyses for element contents and isotopic ratios. Solid Earth Sci. 1 (1), 5–27.
Linnen, R., 1998. The solubility of Nb-Ta-Zr-Hf-W in granitic melts with Li and Li + F: Constraints for mineralization in rare metal granites and pegmatites. Econ. Geol. 93, 1013–1025.
Linnen, R., Keppler, H., 1997. Columbite solubility in granitic melts: Consequences for the enrichment and fractionation of Nb and Ta in the Earth's crust. Contrib. Mineral. Petrol. 128 (2–3), 213–227.
Liu, Y.S., Hu, Z.C., Gao, S., Gunther, D., Xu, J., Gao, C.G., Chen, H.H., 2008. In situ analysis of major and trace elements of anhydrous minerals by LA-ICP-MS without applying an internal standard. Chem. Geol. 257 (1–2), 34–43.
London, D., 2014. A petrologic assessment of internal zonation in granitic pegmatites. Lithos 184-187, 74–104.
London, D., Kontak, D.J., 2012. Granitic Pegmatites: Scientific Wonders and Economic Bonanzas. Elements 8, 257–261.
Marchal, K., Simmons, W., Falster, A., Webber, K., 2014. Geochemistry, mineralogy, and evolution of Li-Al micas and feldspars from the Mount Mica Pegmatite, Maine, USA. Can. Mineral. 52, 221–233.
Ning, S., Wang, F., Xue, W., Zhou, T., 2017. Geochemistry of the Baoshan pluton in the Tongling region of the lower Yangtze River Belt. Geochimica 46, 397–412 (in Chinese with English abstract).
Oyarzábal, J., Galliski, M.Á., Perino, E., 2009. Geochemistry of K-feldspar and muscovite in rare-element pegmatites and granites from the Totoral Pegmatite Field, San Luis, Argentina. Resour. Geol. 59 (4), 315–329.
Rickers, K., Thomas, R., Heinrich, W., 2006. The behavior of trace elements during the chemical evolution of the H_2O-, B-, and F-rich granite-pegmatite-hydrothermal system at Ehrenfriedersdorf, Germany: a SXRF study of melt and fluid inclusions. Mineral. Deposita 41, 229–245.
Roda-Robles, E., Pesquera Peréz, A., Velasco Roldán, F., 1995. Micas of the muscovite-lepidolite series from the fregeneda pegmatites (Salamanca, Spain). Mineral. Petrol. 55, 145–157.
Shearer, C.K., Papike, J.J., Jolliff, B.L., 1992. Petrogenetic links among granites and pegmatites in the Harney Peak rare-element granite-pegmatite system, Black Hills, South Dakota. Can. Mineral. 30, 785–809.
Thomas, R., Davidson, P., 2016. Revisiting complete miscibility between silicate melts and hydrous fluids, and the extreme enrichment of some elements in the supercritical state - Consequences for the formation of pegmatites and ore deposits. Ore Geol. Rev. 72, 1088–1101.
Thomas, R., Webster, J.D., Heinrich, W., 2000. Melt inclusions in pegmatite quartz: complete miscibility between silicate melts and hydrous fluids at low pressure. Contrib. Mineral. Petrol. 139, 394–401.
Thomas, R., Förster, H.-J., Heinrich, W., 2003. The behaviour of boron in a peraluminous granite-pegmatite system and associated hydrothermal solutions: a melt and fluid-inclusion study. Contrib. Mineral. Petrol. 144, 457–472.
Van Lichtervelde, M., Grégoire, M., Linnen, R.L., Béziat, D., Salvi, S., 2008. Trace element geochemistry by laser ablation ICP-MS of micas associated with Ta mineralization in the Tanco pegmatite, Manitoba, Canada. Contrib. Mineral. Petrol. 155, 791–806.
Veksler, I.V., 2004. Liquid immiscibility and its role at the magmatic–hydrothermal transition: a summary of experimental studies. Chem. Geol. 210, 7–31.
Veksler, I.V., Thomas, R., 2002. An experimental study of B-, P-and F-rich synthetic granite pegmatite at 0.1 and 0.2 GPa. Contrib. Mineral. Petrol. 143 (6), 673–683.
Veksler, I.V., Thomas, R., Schmidt, C., 2002. Experimental evidence of three coexisting immiscible fluids in synthetic granitic pegmatite. Am. Mineral. 87 (5–6), 775–779.
Wang, H., Li, P., Ma, H., Zhu, B.Y., Qiu, L., Zhang, X.Y., Dong, R., Zhou, K.L., Wang, M., Wang, Q., Yan, Q.H., Wei, X.P., He, B., Lu, H., Gao, H., 2017a. Discovery of the Bailongshan Superlarge Lithium-Rubidium Deposit in Karakorum, Hetian, Xinjiang, and its Prospecting Implication. Geotecton. Metallog. 4 (6), 1053–1062 (in Chinese with English abstract).
Wang, F., Ge, C., Ning, S., Nie, L., Zhong, G., White, N., 2017b. A new approach to LA-ICP-MS mapping and application in geology. Acta Petrol. Sin. 33, 3422–3436 (in Chinese with English abstract).
Wang, R.C., Xie, L., Zhu, Z.Y., Hu, H., 2019. Micas: Important indicators of granite-pegmatite-related rare-metal mineralization. Acta Petrol. Sin. 35 (1), 69–75 (in Chinese with English abstract).
Wang, H., Gao, H., Yan, Q.-H., Xu, Y.-G., Zhang, X.-Y., Zhou, K., Dong, R., Li, P., 2020. Geology and Geochronology of the superlarge-sized Bailongshan Li-Rb-(Be) rare-metal pegmatite deposit in the West Kunlun Orogenic Belt, NW China. (Submitted to Lithos).
Xiao, W.J., Windley, B.F., Chen, H.L., Zhang, G.C., Li, J.L., 2002. Carboniferous-Triassic subduction and accretion in the western Kunlun, China: Implications for the collisional and accretionary tectonics of the northern Tibetan Plateau. Geology 30, 295–298.
Xiao, W., Han, F., Windley, B.F., Yuan, C., Zhou, H., Li, J., 2003. Multiple Accretionary orogenesis and episodic growth of continents: insights from the Western Kunlun Range, Central Asia. Int. Geol. Rev. 45, 303–328.
Xiao, X., Zhou, T.-F., White, N.C., Zhang, L.-J., Fan, Y., Wang, F.-Y., Chen, X.-F., 2018. The formation and trace elements of garnet in the skarn zone from the Xinqiao Cu-S-Fe-Au deposit, Tongling ore district, Anhui Province, Eastern China. Lithos 302-303, 467–479.
Yan, Q.-H., Qiu, Z.-W., Wang, H., Wang, M., Wei, X.-P., Li, P., Zhang, R.-Q., Li, C.-Y., Liu, J.-P., 2018. Age of the Dahongliutan rare metal pegmatite deposit, West Kunlun, Xinjiang (NW China): Constraints from LA-ICP-MS U-Pb dating of columbite-(Fe) and cassiterite. Ore Geol. Rev. 100, 561–573.
Yin, R., Han, L., Huang, X.-L., Li, J., Li, W.-X., Chen, L.-L., 2019. Textural and chemical variations of micas as indicators for tungsten mineralization: evidence from highly evolved granites in the Dahutang tungsten deposit, South China. Am. Mineral. 104 (7), 949–965.
Yin, R., Huang, X.-L., Xu, Y.-G., Wang, R.-C., Wang, H., Yuan, C., Ma, Q., Sun, X.-M., Chen, L.-L., 2020. Mineralogical Constraints on the Magmatic–Hydrothermal Evolution of Rare-Elements Deposits in the Bailongshan Granitic Pegmatites. Lithos, Xinjiang, NW China Lithos 352-353, 105208.
Zaraisky, G.P., Korzhinskaya, V., Kotova, N., 2010. Experimental studies of Ta_2O_5 and columbite-tantalite solubility in fluoride solutions from 300 to 550 °C and 50 to 100 MPa. Mineral. Petrol. 99, 287–300.
Zhang, Y., Niu, Y., Hu, Y., Liu, J., Ye, L., Kong, J., Duan, M., 2016. The syncollisional granitoid magmatism and continental crust growth in the West Kunlun Orogen, China-evidence from geochronology and geochemistry of the Arkarz pluton. Lithos 245, 191–204.
Zhang, C.-L., Zou, H.-B., Ye, X.-T., Chen, X.-Y., 2019. Tectonic evolution of the West Kunlun Orogenic Belt along the northern margin of the Tibetan Plateau: Implications for the assembly of the Tarim terrane to Gondwana. Geosci. Front. 10, 973–988.
Zhou, B., Sun, Y.X., Kong, D.Y., 2011. Geological features and prospecting potential of rare metallic deposits in the Dahongliutan region, Xinjiang. Acta Geologica Sichuan 31 (3), 288–292 (in Chinese with English abstract).
Zhu, Z.-Y., Wang, R.-C., Che, X.-D., Zhu, J.-C., Wei, X.-L., Huang, X., 2015. Magmatic-hydrothermal rare-element mineralization in the Songshugang granite (northeastern Jiangxi, China): Insights from an electron-microprobe study of Nb-Ta-Zr minerals. Ore Geol. Rev. 65 (4), 749–760.